ACCEPTED FOR PUBLICATION IN APJ; DECEMBER 13, 2010
Preprint typeset using LaTeX style emulateapj v. 11/10/09

MODELING THE MAGNETIC FIELD IN THE GALACTIC DISK USING NEW ROTATION MEASURE OBSERVATIONS FROM THE VERY LARGE ARRAY

C.L. VAN ECK[1], J.C. BROWN[1], J.M. STIL[1], K. RAE[1], S.A. MAO[2,3], B.M. GAENSLER[4], A. SHUKUROV[5], A.R. TAYLOR[1], M. HAVERKORN[6,7], P.P. KRONBERG[8,9], N.M. MCCLURE-GRIFFITHS[3]
1. Dept. Physics & Astronomy, University of Calgary, T2N 1N4, Canada
2.Harvard-Smithsonian Center for Astrophysics, Cambridge, MA 02138, USA
3. Australia Telescope National Facility, CSIRO Astronomy and Space Science, PO Box 76, Epping, NSW 1710, Australia
4. Sydney Institute for Astronomy, School of Physics, The University of Sydney, NSW 2006, Australia
5. School of Mathematics and Statistics, University of Newcastle, Newcastle upon Tyne, NE1 7RU, UK
6. ASTRON, Oude Hoogeveensedijk 4, 7991 PD Dwingeloo, The Netherlands
7. Leiden Observatory, Leiden University, P.O. Box 9513, 2300 RA Leiden, The Netherlands
8. Department of Physics, University of Toronto, 60 St. George Street, Toronto M5S 1A7, Canada and
9. Los Alamos National laboratory, M.S. T006, Los Alamos NM 87545 USA
Accepted for publication in ApJ; December 13, 2010

ABSTRACT

We have determined 194 Faraday rotation measures (RMs) of polarized extragalactic radio sources using new, multi-channel polarization observations at frequencies around 1.4 GHz from the Very Large Array (VLA) in the Galactic plane at $17^\circ \leq l \leq 63^\circ$ and $205^\circ \leq l \leq 253^\circ$. This catalog fills in gaps in the RM coverage of the Galactic plane between the Canadian Galactic Plane Survey and Southern Galactic Plane Survey. Using this catalog we have tested the validity of recently-proposed axisymmetric and bisymmetric models of the large-scale (or regular) Galactic magnetic field, and found that of the existing models we tested, an axisymmetric spiral model with reversals occurring in rings (as opposed to along spiral arms) best matched our observations. Building on this, we have performed our own modeling, using RMs from both extragalactic sources and pulsars. By developing independent models for the magnetic field in the outer and inner Galaxy, we conclude that in the inner Galaxy, the magnetic field closely follows the spiral arms, while in the outer Galaxy, the field is consistent with being purely azimuthal. Furthermore, the models contain no reversals in the outer Galaxy, and together seem to suggest the existence of a single reversed region that spirals out from the Galactic center.

Subject headings: Galaxy: structure — ISM: magnetic fields — polarization

1. INTRODUCTION

While the importance of the Galactic magnetic field is undisputed – ranging from star formation to large-scale galactic dynamics – much remains unknown about how the field is generated or how it is evolving. The only way to address these questions is to fully understand the present overall structure of the field, which is an essential constraint to proposed evolutionary models of the field.

One observation central to the study of the Galactic magnetism is that of the Faraday rotation measure (RM). As a linearly polarized electromagnetic wave propagates through a region containing free thermal electrons and a magnetic field, such as the interstellar medium, the plane of polarization will rotate through the process known as Faraday rotation. The amount of rotation, $\Delta\phi$ [rad], experienced by a wave of a given wavelength, λ [m], is given by

$$\Delta\phi = 0.812\lambda^2 \int_{\text{source}}^{\text{receiver}} n_e \mathbf{B}\cdot\mathrm{d}\mathbf{l}, \qquad (1)$$

where n_e [cm^{-3}] is the electron density, $\mathbf{B}[\mu\text{G}]$ is the magnetic field, d$\mathbf{l}$ [pc] is the path length element. Assuming that the polarization angle at the source, $\phi_\circ$, is the same for all emitted wavelengths, that Faraday rotation is the only mechanism acting on the polarization angle, and that the source of interest is the only source contributing polarized emission along the line of sight, then the detected polarization angle, ϕ, is a linear function of the square of the wavelength through the relationship

$$\phi = \phi_0 + \lambda^2 \mathrm{RM}, \qquad (2)$$

where RM is the Rotation Measure, defined from equation 1. As a result, measuring the polarization angle at several wavelengths for a given source can provide a simple determination of the rotation measure for that line of sight, provided that there is no internal Faraday dispersion by turbulent magnetic fields (see e.g. Sokoloff et al. 1998).

If there exist multiple polarized emitting regions along a line of sight, for example, from different regions within the primary source, or from different regions within the interstellar medium of the Galaxy itself, or turbulent cells with random field directions, each emitting region will have a different RM contributing to the final detected RM, otherwise known as *RM components*. A technique developed by Brentjens & de Bruyn (2005), known as RM Synthesis, is able to extract the RM components using Fourier transforms. However, there remains the difficulty of determining where along the line of sight the components originate, and how the components 'add' is highly dependent on the instrumentation used to detect the signals. Therefore, it is more straightforward to use single component RM sources to probe the magnetic field within the Galaxy. The two sources most often used are pulsars (within the Galaxy) and compact extragalactic sources (EGS). We note that the higher the angular density of the observed probes, the greater the capacity to identify and separate the ordered and random field components.

For the purposes of modeling, the Galactic magnetic field is often, and somewhat arbitrarily, divided into two components: a large-scale or regular component, $\mathbf{B}_u$, with spatial scales on

clvaneck@ucalgary.ca; jocat@ras.ucalgary.ca

the order of a few kpc, and a turbulent or random component $\mathbf{B}_r$, with spatial scales on the order of tens of pc (Ruzmaikin et al. 1988), with significant different spatial scales observed between and within the spiral arms (Haverkorn et al. 2006, 2008). Furthermore, the regular component is observed to be concentrated in the disk (Simard-Normandin & Kronberg 1980), with a dominant azimuthal component, some radial component (thus indicating a spiral field), and a weak vertical or z component (Mao et al. 2010).

Additionally, recent work has focused on developing and testing competing models, and determining the existence of large scale reversals in the magnetic field. Magnetic field reversals occur where the magnetic field direction completely reverses over a short change in radius and/or azimuth within the disk of the Galaxy. The number of reversals depends on the interpretation of the existing RM data and is presently a very controversial subject (e.g. Brown & Taylor 2001; Weisberg et al. 2004; Vallée 2005; Han et al. 2006; Brown et al. 2007; Sun et al. 2008; Vallée 2008; Men et al. 2008; Jansson et al. 2009; Kronberg & Newton-McGee 2009; Nota & Katgert 2010). Models of the Galactic magnetic field are generally classified as axisymmetric spiral (ASS), which requires symmetry under the same rotation of the disk by π around the Galactic center, bisymmetric spiral (BSS), which requires anti-symmetry under rotation by π, or mixed spiral structure (MSS), which contain both ASS and BSS components (Beck et al. 1996). Most models are made to follow the spiral arm structure of the Galaxy since an approximate alignment of the regular magnetic fields and spiral arms is commonly observed in external galaxies (e.g. Beck 2007).

For all of these models, sufficient numbers of low-latitude, high quality RM data in key regions have been lacking. While the recent catalog of Taylor et al. (2009) significantly increases the number of published EGS RM sources across the entire sky, those in the plane lack adequate reliability for modeling the magnetic field in the disk (see section 2).

In this paper, we present our new low-latitude EGS RM catalog derived from new observations from the Very Large Array (VLA), filling in gaps in Galactic plane coverage in quadrant 1 (Q1; $0^\circ < l < 90^\circ$) and quadrant 3 (Q3; $180^\circ < l < 270^\circ$). We use these data to further discriminate between three popular models investigated by Sun et al. (2008). We then combine these data with previous observations to develop magnetic field models for three separate sectors of the Galactic disk and find some remarkable consistencies between the sectors, suggesting global features of the field.

2. OBSERVATIONS

Two recent projects have produced catalogues for several hundred EGS RMs in the plane of the Galaxy: the Canadian Galactic Plane Survey (CGPS; Taylor et al. 2003; Brown et al. 2003a) and the Southern Galactic Plane Survey (SGPS; Haverkorn et al. 2006; Brown et al. 2007). While covering a significant fraction of the Galactic disk, these surveys left two gaps in the EGS RM coverage of the Galactic plane as shown in Figure 1.

In June and July of 2008, we carried out 48 hours of observing with the VLA under the program AM959 to fill in the gaps in EGS RMs between the CGPS and SGPS. Observations done on June 8 and June 20 were carried out in DnC configuration where we gave priority to low-declination sources, while the remaining observations (carried out on June 29, July 4, July 5, July 10, and July 12) were in D configuration. Our observations in Q1 were confined to $17^\circ \leq l \leq 43^\circ$, $-3^\circ \leq b \leq 3^\circ$ and $43^\circ < l \leq 63^\circ$, $-4^\circ \leq b \leq 4^\circ$ and in Q3 with $205^\circ \leq l \leq 253^\circ$, $-5^\circ \leq b \leq 5^\circ$. We increased the latitude coverage for higher longitudes to maximize the number of sources we had, while still maintaining lines-of-sight largely confined within the Galactic disk under the assumptions of a Galactic radius of 20 kpc and a warm ionized medium scale height of 1.8 kpc (Gaensler et al. 2008).

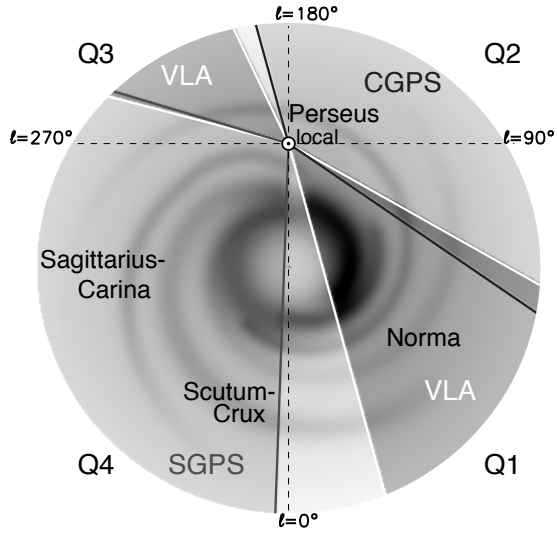

FIG. 1.— View of the Milky Way from above the north Galactic pole illustrating the main survey regions of extragalactic rotation measures used in this paper. The grey scale background is the electron density distribution model of Cordes and Lazio (2002). The dark lines are the boundaries of the regions observed by the CGPS and SGPS, while the white lines denote the 2 areas targeted by the VLA data used for this project. The dashed lines show the delineations between the Galactic quadrants (Q1 - Q4).

The sources observed were selected from the NRAO-VLA Sky Survey (NVSS; Condon et al. 1998) with the following criteria: 1) they were unresolved, having an NVSS fitted major axis of less than 60 arcseconds; 2) their linearly polarized flux as given in the published NVSS catalogue was greater than 2 mJy (bias corrected); 3) they had a minimum fractional polarization of 2% in Q3 or 1% in Q1. We used a different minimum fractional polarization in Q1 than in Q3 to minimize selection against high RMs as a result of bandwidth depolarization in the NVSS. Using these criteria, we observed a total of 486 sources.

We observed each source in spectral-line mode, using an integration time of at least 2 minutes in two separate 25 MHz bands, each with 7 channels, giving 14 wavelengths and 14 corresponding polarization angles. For our first observations of 76 sources (June 8), we centered the two bands at 1365 MHz and 1515 MHz. The 1515 MHz band was unusable due to radio frequency interference (RFI), so the sources from these observations were discarded. For all subsequent sources, we used bands centered at 1365 MHz and 1485 MHz.

When possible, we observed a primary flux calibrator (3C286 or 3C138) in both observing bands at the beginning and the end of an observation run. For the duration of a given run, we observed sources in groups of 15-18 sources in one band within a 1 hour window. Every hour, we visited a phase calibrator that was usually within 10 degrees of the target group. We then repeated the observations of the target group in the second band (i.e. band A: phase calibrator $\rightarrow$ band A: target group: $\rightarrow$ band A: phase calibrator $\rightarrow$ band B: phase calibrator $\rightarrow$ band B: target group $\rightarrow$ band B: phase calibrator $\rightarrow$ *repeat*).

Data reduction was carried out using AIPS software. The AIPS task IMAGR was used to do imaging and cleaning, which was performed down to the noise level for each source (between 0.6 mJy and 1.1 mJy). CLEAN boxes were defined tightly around the target source to prevent cleaning of sidelobes of the dirty beam. Baselines shorter than 1 kλ were excluded to reduce extended emission (equalling about 30% of all baselines). No additional weighting was used in the UV plane. Polarization calibration was done using the standard calibration method as described in the AIPS manual, using 3C286 as a polarization calibrator. We note that polarization calibration in AIPS can only be done on one channel at a time. Thus, each of the 14 channels was calibrated and imaged separately, using 10″ pixels and a 50″ clean beam. The polarization angle and polarized intensity for each channel (i.e. at each wavelength) were then extracted from the source pixel with the greatest channel-averaged polarized intensity (determined by averaging the polarized intensity from the individual channels).

From these polarization angles, the RM is calculated using a least-squares fit to the polarization angle versus wavelength-squared plot, as reflected by equation (2). Since polarization angles are only defined between 0 and π, all polarization angle measurements are subject to an issue of '$n\pi$ ambiguity'. To address this issue within our data, we have used the algorithm used by Brown et al. (2003a) to determine the relative angles between channels within each band separately. To determine the $n\pi$ between the two 25 MHz bands observed, best fit lines were determined separately for each band and extrapolated out to the other band. If the determined value for n as determined by the separate bands was different, the source was discarded. The bands were then adjusted by the appropriate $n\pi$, and the RM was determined from the slope of the best fit line using both bands together (see Figure 2). The error in RM was determined as the error in slope of the 2-band best fit line.

In order to be considered a reliable RM value, the source had to have a 'probability-of-fit' for the least-squares fit of polarization angle versus λ^2 be greater than the standard value of 10%. In addition, the source also had to pass two more tests that were designed to confirm that the $n\pi$ algorithm worked consistently and that the source has a *single* RM value (or, alternatively, a consistent, dominant RM component). First, we confirmed that the 4 pixels adjacent to the central pixel (above, below, and to the sides) had similar RMs. Sources with the mean RM of the 4 adjacent pixels greater than 2σ different than the central pixel RM value were rejected. Second, we confirmed that the fractional polarization (linearly polarized intensity divided by Stokes I) was constant with λ^2. While the presence of multiple RM components may still combine to produce linear behavior in polarization angle versus λ^2 over small wavelength ranges (thereby leading to incorrect calculated RMs), multiple components are also expected to produce nonlinear behavior in polarized *intensity* versus λ^2 (Goldstein & Reed 1984; Farnsworth, Rudnick, & Brown 2011). By contrast, a single (or at least, dominant) RM component is expected to have polarized intensity versus λ^2 be roughly constant. Therefore, we used a second 'probability-of-fit' test (also at the 10% level) of the fractional polarization values versus λ^2 against a line with zero slope and offset equal to the mean fractional polarization. Sources failing this test were also discarded.

Using this method, we determined reliable RMs for 194

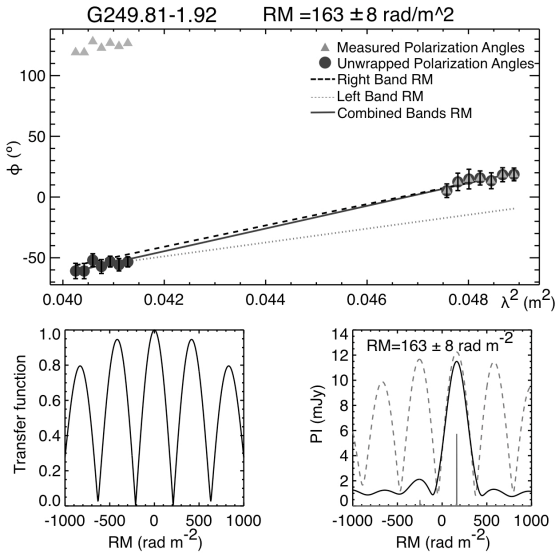

FIG. 2.— Determining rotation measures for the VLA observations. Top: A demonstration of the polarisation angle $n\pi$ determination method for rotation measure calculations as described in the text. The triangles are the observed angles, circles are the adjusted angles. The dashed (dotted) lines are the extrapolations of the right (left) band, and are used to determine the inter-band $n\pi$ adjustment needed to produce the best fit. The solid line is the rotation measure determined using both bands after applying the algorithm. Bottom left: The rotation measure transfer function for RM synthesis resulting from the 14-channel sampling. Bottom right: The RM Synthesis result for the same source. The light dotted line is the raw spectrum, the grey solid line is the RM CLEAN component spectrum, and the solid black line is the final CLEANed spectrum.

sources as documented in Table 1, and illustrated in Figure 3. As a consistency check of this catalog, we have compared our RMs to the following two determinations of RMs for the same sources. In addition to the linear fitting method described above, we also calculated RMs from the same data using RM synthesis, as outlined by Brentjens & de Bruyn (2005), which employs Fourier transforms to determine the RM. The resulting RM spectra were processed with the RM CLEAN algorithm, as outlined in Heald et al. (2009). The values found with the synthesis and linear fitting methods are in complete agreement, with the variation between the two methods much less than the stated error in RM. The RM synthesis results are included in Table 1.

The second comparison was with the RM catalog produced directly from the original NVSS observations by Taylor et al. (2009), where RMs are calculated using observations at 1364.9 and 1435.1 MHz. Their method used two polarization angle measurements, combined with depolarization information to solve the half-rotation ambiguity. Figure 4 is a comparison of RMs of sources for which there are values from both surveys. It is clear that some of the sources have RMs determined by the two techniques that differ by $\sim$650 rad m^{-2}. A 1π ambiguity introduces a $\sim$650 rad m^{-2} offset in a RM determined by Taylor et al. (2009). For our data, however, a 1π ambiguity would require an actual RM of greater than 10,000 rad m^{-2}. Consequently, it is certain that the offset sources in Figure 4 reflect the 1π ambiguity of the Taylor et al. (2009) algorithm. The linear correlation coefficient for all 146 matched sources is 0.20, but this rises to 0.96 when the 13 offset sources are removed from the calculation. This correlation is much higher than that found by Mao et al. (2010; 0.39 in the North, and 0.36 in the South), likely because our data includes a much larger range of RMs which reduces the

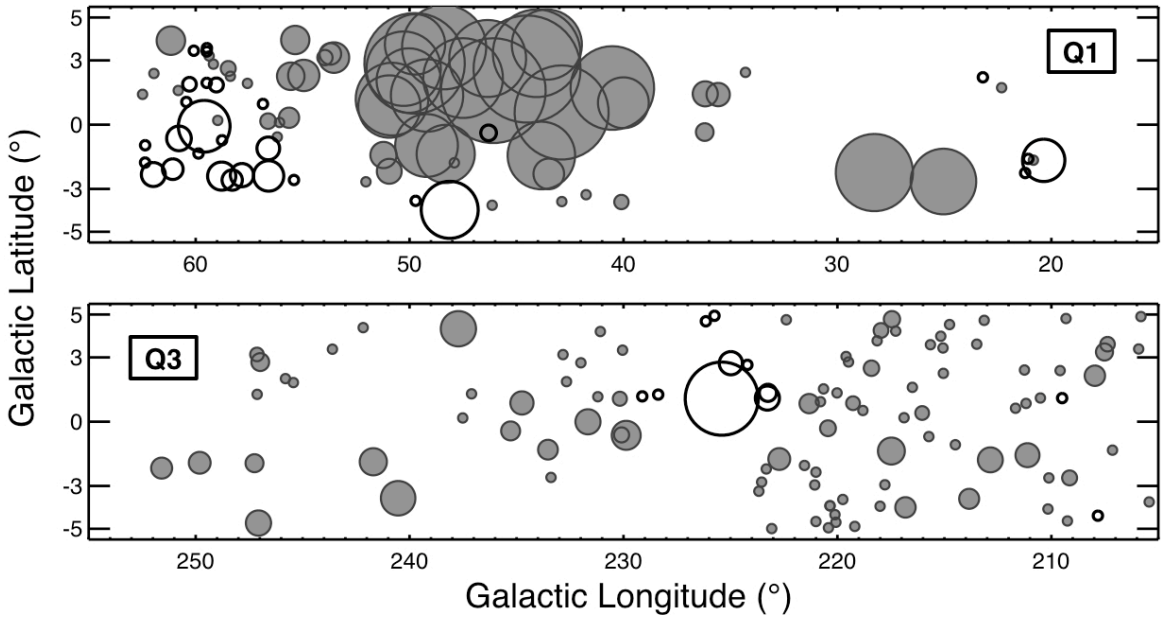

FIG. 3.— Rotation measure sources from Table 1. Grey filled sources indicate positive rotation measure and black open symbols indicate negative rotation measures; diameters of symbols are linearly proportional to the magnitude of RM truncated between 100 and 600 rad m^{-2} so that sources with |RM| $<$ 100 rad m^{-2} are set to 100 rad m^{-2}, and those with |RM| $>$ 600 rad m^{-2} are set to 600 rad m^{-2}. The top panel represents sources from Galactic quadrant 1 (Q1), while the bottom panel represents sources from Galactic quadrant 3 (Q3).

effect of random errors. As well as the $\sim$650 rad m^{-2} offset for a few sources, there are additional differences between our RM values and those of Taylor et al. (2009). As demonstrated in Figure 4, their values are systematically lower than ours, with a mean shift of 10 rad m^{-2}. Further, the standard deviation of the differences between their values and ours (neglecting the 1π shifts and differences between sources with large RMs) is 23 rad m^{-2}. Given that we are working in the part of the sky, namely the Galactic disk, where RMs vary significantly over relatively short angular distances, and the fact that we systematically resolve nπ ambiguities more reliably than their technique does in the same part of the sky, there is a significant advantage to using our RM values in our effort to infer magnetic field structure in the plane of the Galaxy. The systematic shift of the RMs inferred from the two techniques, and the variance between the two, undoubtedly indicate errors in one or both of the methods. These errors are worth investigating further, but because they are almost certainly small relative to the real large scale trends in RM in the Galactic plane (the RMs vary systematically by hundreds of rad m^{-2} but the shift and variance are both on the order of 10 rad m^{-2}) they are not important for this study.

3. OBSERVATIONAL DISCRIMINATION OF POPULAR GMF MODELS

Sun et al. (2008) presented a thorough investigation of three models for the Galactic magnetic field which represented a culmination of a variety of inputs from earlier popular models. The three models they present are a BSS model and two ASS models: one with magnetic field reversals following the spiral arms of the Galaxy (ASS+ARM), and the other with reversals in rings of constant radius (ASS+RING). Part of the efforts by Sun et al. (2008) included an exploration of how well these models fit pulsar RMs (Han et al. 1999) and previously published extragalactic RMs from the Canadian Galactic Plane Survey (Brown et al. 2003a), the Southern Galactic Plane Survey (Brown et al. 2007), and a sample of RMs along sight lines close to the Galactic centre (Roy et al. 2005). Using high-latitude CGPS data (see Rae & Brown 2011), Sun et al. (2008) show an RM latitude profile between $100^\circ < \ell < 120^\circ$ (their Figure 12) which clearly suggests that only the ASS+RING or ASS+ARM models are good contenders, particularly in this longitude range. However, as stated by Jansson et al. (2009), filling in the gaps of the EGS RM data in the disk is essential to properly discern between the models. With our new data, we are now in a position to contribute to the assessment of these three models.

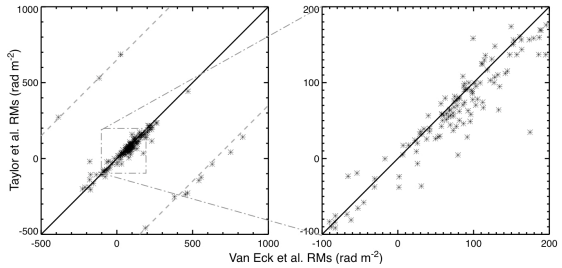

FIG. 4.— Comparison of NVSS RMs calculated by Taylor et al. (2009) to our new VLA RMs presented here. The solid line is the 1:1 line corresponding to complete agreement. In the left panel, the dashed lines are parallel to the 1:1 line with the $\pm$650 rad m^{-2} offset that a $\pm\pi$ RM ambiguity error would add to an RM determined by the Taylor et al. (2009) algorithm (as they discuss, the value of the shift from a 1π ambiguity error is determined by the two wavelengths for which polarization information is available for the NVSS catalog). Roughly 5% of the corresponding sources have a $\pm$650 rad m^{-2} offset. Given that a 1π RM ambiguity error in a source determined from our algorithm would give a significantly larger offset, we attribute the offsets of this limited number of sources to unresolved ambiguities in those specific Taylor et al. (2009) sources. The right panel is an enlargement of part of the left panel, showing the scatter of the points about the 1:1 curve. There is a slight systematic shift of the Taylor et al. (2009) RMs towards more negative values, with a 23 rad m^{-2} standard deviation of the difference between the two.

Figure 5 shows our RMs in the Q1 and Q3 regions seperately, with the predictions of the models from Sun et al. (2008) overlaid. As shown, the three models have very different predictions in EGS RMs in Q1 where the reversal's tangent point occurs, but, as could be expected, the three models are very similar in Q3. Our data from Q1 is most consistent with the ASS+RING model, particularly between $40^\circ < \ell < 60^\circ$, where the RMs being generally positive and decreasing with increasing longitude. The other two models predict negative RMs in this region.

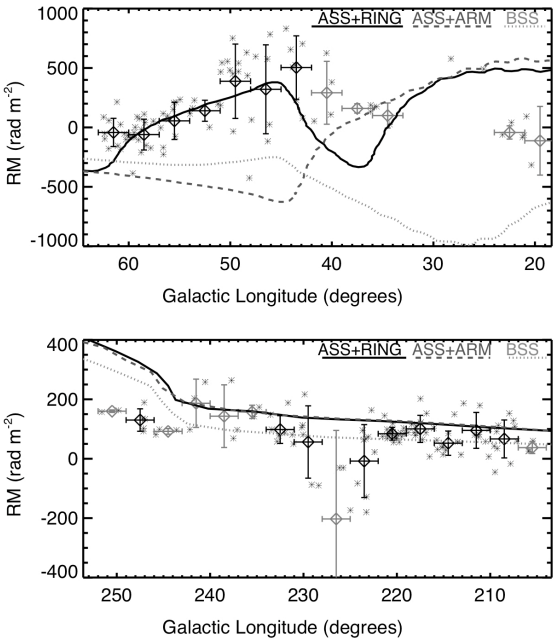

FIG. 5.— Rotation measure versus Galactic longitude for sources in quadrant 1 (upper panel) and quadrant 3 (lower panel). The diamonds are 3 degree-averaged independent bins (error bars are the bin width and standard deviation of the mean) of the individual sources (shown as black asterisks). Bins shown in black contain at least 5 sources; bins shown in grey contain between 2 and 4 sources. The three lines show the predictions of the models investigated by Sun et al. (2008) taken directly from their Figure 10, as specified in the upper right corner of each panel.

The ASS+RING model is also more consistent with dynamo models where the axisymmetric solutions of the mean-field dynamo equations in a thin disk are of the form $\mathbf{B}_u = Q(R)\mathbf{b}(z,R)$, where $Q(R)$ describes the field strength along the radius, R, and $\mathbf{b}$ describes the field distribution perpendicular to the disk (with R and z the cylindrical coordinates; Ruzmaikin et al. 1985; Poezd et al. 1993). A reversal of an axisymmetric field occurs at $R = R_0$ where $Q(R_0) = 0$ (i.e. on a circle). We note, however, that none of the models discussed here fit the observations as well as would be desired. The idea that the field is not as simple as an axisymmetric or bisymmetric spiral has been discussed extensively by Men et al. (2008).

4. MULTI-SECTOR MODEL OF THE MAGNETIC FIELD IN THE GALACTIC DISK

As discussed by Jansson et al. (2009), none of the global models of the large-scale magnetic field studied to date adequately reproduce the data across the entire disk. In the previous section, we determined that the ASS+RING described by Sun et al. (2008) fit best for our Q1 data. This model, however, is quite different than that of Brown et al. (2007) that was quite successful in reproducing the data in Q4. Conversely, the model of Brown et al. (2007) does not do well in Q1, as demonstrated by Jansson et al. (2009). Furthermore, as the CGPS observations have progressed, it has become evident that a simple spiral model in the outer Galaxy is not consistent with the data (Rae & Brown 2011). We also note that Shukurov (2005) suggested that the reversal in the Milky Way may be localized in a region within several kiloparsecs near the Sun. If this is the case, an entirely different type of analysis is required, such as what we propose below.

While many other recent works have focused on building an empirical model of the large-scale magnetic field for the entire Galactic disk (e.g. Weisberg et al. 2004; Han et al. 2006; Vallée 2008) or have looked at only specific regions of the disk (e.g. Brown et al. 2007; Nota & Katgert 2010), we chose to take a 'hybrid' approach. Our modeling work examines the entire Galactic disk, but in 3 separate sectors to see if we can determine any common features or structure. We purposely do not apply any 'boundary matching' conditions between the sectors in order to facilitate independent results for each of the three sectors examined. It was our intention to see if there was any commonality amongst the different sectors that could be arrived at independently. With this in mind, we chose the following three sectors, as illustrated in Figure 6: Sector A isolates the outer Galaxy (excluding the local arm) and spans most of quadrants 2 and 3 (Q2 and Q3); Sector B spans all of quadrant 4 (Q4) which includes the half of the inner Galaxy with significant lines of sight along the spiral arms; Sector C spans all of quadrant 1 (Q1) which includes the half of the inner Galaxy that has lines-of-sight primarily perpendicular to the spiral arms.

The method we use is described by Brown et al. (2007) and in greater detail in Brown (2002). In summary, we attempt to empirically reproduce the observed RMs of both pulsars and EGS using the electron density of Cordes & Lazio (2002, hereafter NE2001), and various magnetic field models. We acknowledge that this modeling technique is limited in the sense that it relies heavily on the validity of the assumed electron density and magnetic field models. However, the NE2001 model reproduces well the dispersion measures of pulsars and observed spiral structure at low latitudes, though it does have limited value at mid to high latitudes (Gaensler et al. 2008). In our case, we are only interested in low latitudes, so with all other caveats, we have chosen to use this electron density model. While it is possible to construct magnetic field models using a constant electron density (e.g. Nota & Katgert 2010), such models put all of the structure of the RMs into the magnetic field. Instead, we were interested in attempting to explore the relationship between the spiral arms and the magnetic field.

The magnetic field models investigated here are defined in terms of several regions with distinct magnetic field configurations (direction and magnetic pitch angle), as illustrated in Figure 6, but the strength and direction of the field are outputs obtained minimizing the difference between the data and the model through linear inversion theory (Menke 1984). By definition within the model, positive fitted field strengths correspond to a counter-clockwise field (as viewed from the North Galactic pole) within that region, while negative fitted field values correspond to a clockwise direction. In addition, since the goal of our modeling is to explore the large-scale field, we ignore the small-scale clumps and voids of NE2001, and use only the thin, thick, and spiral arm components.

In addition, we placed the following restrictions on all of the models we investigated. First, the magnetic field for

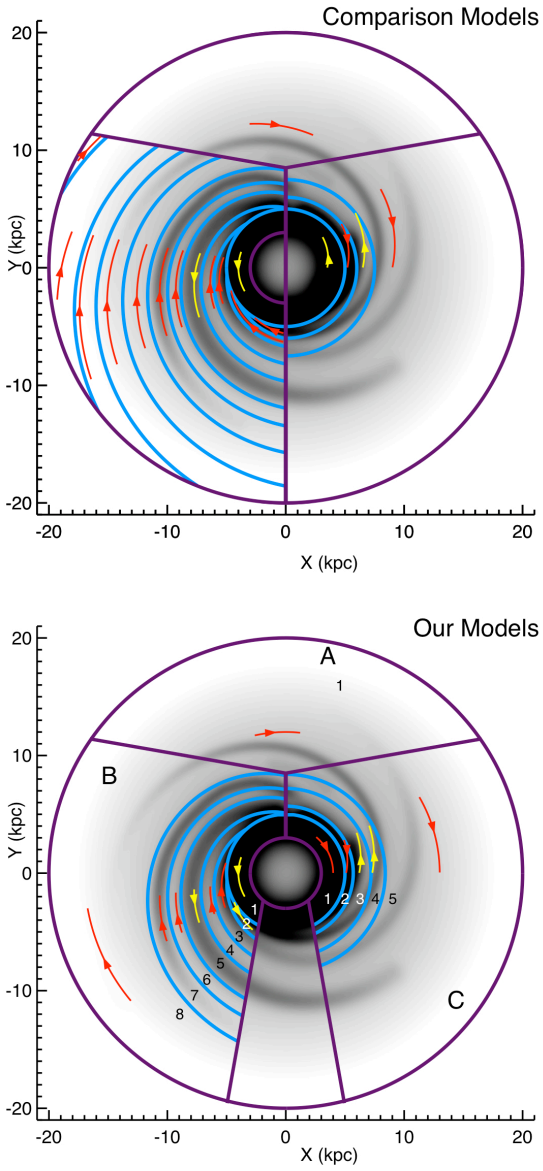

FIG. 6.— Comparison of magnetic field regions and delineation for the 3 sectors investigated in this paper. Top panel shows the 3 sectors with previous or comparative model delineations: Region A: Logarithmic spiral with 11.5° magnetic pitch angle; Region B: Model from Brown et al. (2007); Region C: ASS+RING model from Sun et al. (2008). The bottom panel shows the region delineations and magnetic field directions for our proposed models in the three sectors. The numbers correspond to the regions listed in Table 2. We note that the field directions indicated on the lower panel are an output of the model, and were not assigned *a priori*.

Galactocentric radii $R > 20$ kpc or $R < 3$ kpc was set to zero. Similarly, the field was assumed to be zero for $|z| > 1.5$ kpc. In addition, all models have a circular region containing the molecular ring of the NE2001 electron model (3 kpc $\leq R \leq 5$ kpc) with a circular magnetic field regardless of the geometry being tested in the rest of the Galaxy.

Using the best-fit values for the magnetic field regions in each model (given in Table 2), we are then able to determine the model RMs for each of the observed source locations. To assess the quality of fit of each model, we calculated the root mean square of the residuals in RMs,

$$\langle(\Delta\mathrm{RM})^2\rangle^{1/2} = \langle(\mathrm{RM}_{\mathrm{observed}} - \mathrm{RM}_{\mathrm{model}})^2\rangle^{1/2}, \qquad (3)$$

where the goal was to minimize this value with the modeling. Due to the intrinsic scatter of the EGS RMs and the high angular density of EGS available to us, we smoothed the observed and modeled EGS RMs, as described below, before calculating the $\langle(\Delta\mathrm{RM})^2\rangle^{1/2}$ value.

We used EGS RMs from the data presented here, as well as the SGPS and CGPS data sets. We treated the EGSs as being located at the edge of the model ($R = 20$ kpc). Since we did not wish to investigate the complex nature of the field likely to be found near the Galactic center, we did not use any EGS RM sources within $\pm 10°$ Galactic center and consequently did not use any of the RMs determined by Roy et al. (2005). We also did not consider any vertical structure in our model. Therefore, we removed any sources with a calculated height $|z| > 1.5$ kpc. With these criteria, we were left with 184 of the 194 RMs described in section 2, 142 of the 148 RMs from the SGPS (Brown et al. 2007) and 1020 sources from the CGPS, a total of 1346 EGS sources.

We used 557 pulsar RMs from the following sources: Noutsos et al. (2008), Han et al. (2006), Weisberg et al. (2004), Mitra et al. (2003), Han et al. (1999) and Taylor et al. (1993) where pulsars were selected with $|z| < 1.5$ kpc. For self-consistency, we used distances to the pulsars predicted by the NE2001 model.

The EGS and pulsar RMs were then split by sector as described in the following sections. The primary objective of our modeling is to produce the best-fitting empirical model with the fewest parameters. To that end, we decided to explore the outer Galaxy first, since it can be expected to be the simplest in nature.

4.1. *Model Sector A: The Outer Galaxy (Q2 and Q3)*

We define Sector A to be $100° < \ell < 260°$. In this region, we have RMs for 88 pulsars, and 847 EGS (21 from SGPS, 108 from the catalog in this paper, 718 from CGPS).

As demonstrated by earlier CGPS work, RM data in the outer Galaxy holds no strong evidence for a large-scale reversal (Brown & Taylor 2001; Brown 2002; Brown et al. 2003b). There is some evidence that suggests that the field decays as R^{-1}, consistent with the decay in electron density (Brown et al. 2003b). Since the relationship between the large-scale magnetic field and the electron density has not been formally identified, we investigated several different radial profiles for the large-scale field including R^{-1}, $R^{-1/2}$, $\exp(-R/5\,\mathrm{kpc})$, and $\exp(-R/10\,\mathrm{kpc})$ and constant field strength. All profiles produce similar results in the modeling, as there are not enough pulsar data to effectively constrain the radial profile of the large-scale magnetic field in the outer Galaxy. Therefore, we modeled this region as a single magnetic entity with an R^{-1} decay profile, consistent with earlier observational suggestions. The question we were interested in addressing was whether a spiral field was more or less appropriate than a predominantly azimuthal field. Recent work by Rae & Brown (2011) provides evidence for a very small pitch angle in the outer Galaxy, by determining the value for the 'RM null point' in the outer Galaxy (the longitude where the RMs transition from positive to negative, corresponding to where the magnetic field is, on average, perpendicular to the line of sight) as $\ell = 179° \pm 1°$. We investigated a range of pitch angles and found that those close to zero were clearly preferred as indicated by a minimum in $\langle(\Delta\mathrm{RM})^2\rangle^{1/2}$ at a pitch angle of 0° and a 10% change in $\langle(\Delta\mathrm{RM})^2\rangle^{1/2}$ occurring at a pitch angle of 4°.

In Figure 7, we present the results for a spiral model in-

clined at 11.5°, consistent with the spiral arms of NE2001, and compare the results with the best fit for a purely azimuthal model (magnetic pitch angle of 0°). Both models reproduce the gentle trend of the data to change from positive RM in Q3 to negative RM in Q2. However, the purely azimuthal model minimizes the $\langle(\Delta\mathrm{RM})^2\rangle^{1/2}$ by 30% better than the logarithmic spiral model. Figure 7 also serves to illustrate that the observed 'null point' of the CGPS data clearly occurs close to 180° longitude as predicted by the circular model, implying a field with a very small or even zero pitch angle compared to the spiral arms. This is in contrast with the predicted null of $\ell = 166°$ predicted by the spiral model with the same pitch as the spiral arms (as defined by Cordes & Lazio 2002). The slight shift of the null-point in the data to $\ell > 180°$ is more likely due to small-scale structures such as supernova remnants dominating the line of sight magnetic field at these longitudes (e.g. Kothes & Brown 2009), rather than a spiral field with the opposite 'handedness' to that of the optical spiral arms.

4.2. *Model Sector B: SGPS region (Q4)*

We define Sector B to be $260° < \ell < 360°$, which is slightly smaller than the area modeled by Brown et al. (2007). This region contains 292 pulsars and 121 EGS (all from the SGPS).

For their model, Brown et al. (2007) used the available pulsar RMs combined with new EGS RMs from the SGPS to model the magnetic field within the SGPS region. The model had magnetic regions delineated by the spiral arms of NE2001, with a magnetic pitch angle of 11.5° in all regions, except the 'molecular ring' which is modeled as an azimuthal field. For $R < 3$ kpc or $R > 20$ kpc the field was assumed to be zero, and there was no vertical component assumed for the field. Their field strength was assumed to have a R^{-1} dependence, which facilitated a model with significant difference in strength between the inner and outer Galaxy. This was needed since some of the regions appeared in the modeling region twice – once in the inner Galaxy, and once in the outer Galaxy – as a consequence of the spiral geometry (e.g. the Norma arm in their Figure 4).

Given how well the model of Brown et al. (2007) agreed with the data, we decided to keep much of this model the same. To that end, we merged all separate regions beyond the Sagittarius-Carina arm into one magnetic field region, and redefined the field in this new outer-Galaxy region to be purely azimuthal, and still retained the R^{-1} dependence in this region, consistent with Brown et al. (2003b). However, for the remaining regions in the inner Galaxy, we reverted to a constant field strength, as suggested by Nota & Katgert (2010).

The best-fit magnetic field results for our variation on the Brown et al. (2007) model are virtually indistinguishable from the original. As shown in Figure 8, the $\langle(\Delta\mathrm{RM})^2\rangle^{1/2}$ for our new model is not statistically significantly different from that for the model of Brown et al. (2007). However, the model is less complicated as illustrated in Figure 6. It has 8 regions compared to 9 regions in the original model, and has removed the complexity of the R^{-1} dependence in the inner Galaxy. The reduction in the number of parameters while maintaining a good quality of fit, makes this new model more attractive.

4.3. *Model Sector C: VLA region (Q1)*

We define Sector C to be $0° < \ell < 100°$. In this region, we have 177 pulsar RMs and 378 EGS RMs (302 from CGPS, 76 from our VLA observations).

In this segment of the Galaxy, we used as our starting position the ASS+RING model described by Sun et al. (2008). In particular, we began by assuming that in the inner Galaxy, the magnetic region delineations are circular, but the fields within the regions are spiral. We note a few critical differences between our model and theirs: 1) we use only the smooth components of NE2001 as noted above (Sun et al. used all components); 2) we use a maximum scale height of the field as 1.5 kpc (Sun et al. use 1.0 kpc); 3) we have five separate regions (Sun et al. have four); 4) we use a magnetic pitch angle within the individual regions of 11.5°, except for the innermost region (1C as labeled on Figure 6) and the outermost region (5C), which we define to be azimuthal to be consistent with our work in sectors A and B (Sun et al. used 12° in all regions).

The first region boundary of our model is located at R = 5.0 kpc to correspond to the molecular ring of NE2001. The remaining boundaries were optimized using the $\langle(\Delta\mathrm{RM})^2\rangle^{1/2}$ value as the quality-of-fit measure. The optimized boundary locations were found to be R = 5.8 kpc, R = 7.2 kpc, and R = 8.4 kpc.

For this model, our best fit magnetic field model is predominantly clockwise with a reversed (clockwise) region in the inner Galaxy, as shown in Figure 6. Figure 9 shows a direct comparison to the data and values predicted by the ASS+RING model and our model. When the data are smoothed, our model shows a factor of 4 improvement in the $\langle(\Delta\mathrm{RM})^2\rangle^{1/2}$ over the ASS+RING model.

4.4. *Combining the Sectors*

When we consider our three sectors together, as shown in Figure 10, a picture emerges of a predominantly clockwise Galactic magnetic field with what could be interpreted as single reversed (counter-clockwise) region spiraling out from the Galactic center, as illustrated in Figure 11. According to our analysis, the field in the inner Galaxy has a spiral shape (with a pitch angle estimated here as 11.5°) and is generally aligned with the spiral arms while in the outer Galaxy it is (almost) azimuthal. This is consistent with the observations of Kronberg & Newton-McGee (2009) who suggested explicitly that the Galaxy is a mix of an axisymmetric field in the outer Galaxy and a bisymmetric field in the inner Galaxy. The opposite signs of the two molecular rings may be suggestive of a bisymmetric field originating from the Galactic bar. More data and perhaps a new electron density model containing the bar would be necessary in order to properly investigate this region.

We also note that this 'spiraling-out' reversed region could extend into Q1 at larger Galactic radii, but without any data from pulsars located on the far side of the Galaxy in this region, determining the existence of such a region is not possible. Our model may be considered as something of a zeroth-order approximation; it was constructed in a piece-wise manner, yet there is some consistency across the whole Galactic disk. The discontinuities that occur at the boundaries are a consequence of this and indicate that the actual field configuration cannot be fully modeled using the simple geometries that we have tested. Exploration of more complex geometries will be necessary to improve the boundary matching. However, if such a model significantly increases the number of parameters within the model, additional data will certainly be needed to properly constrain the model.

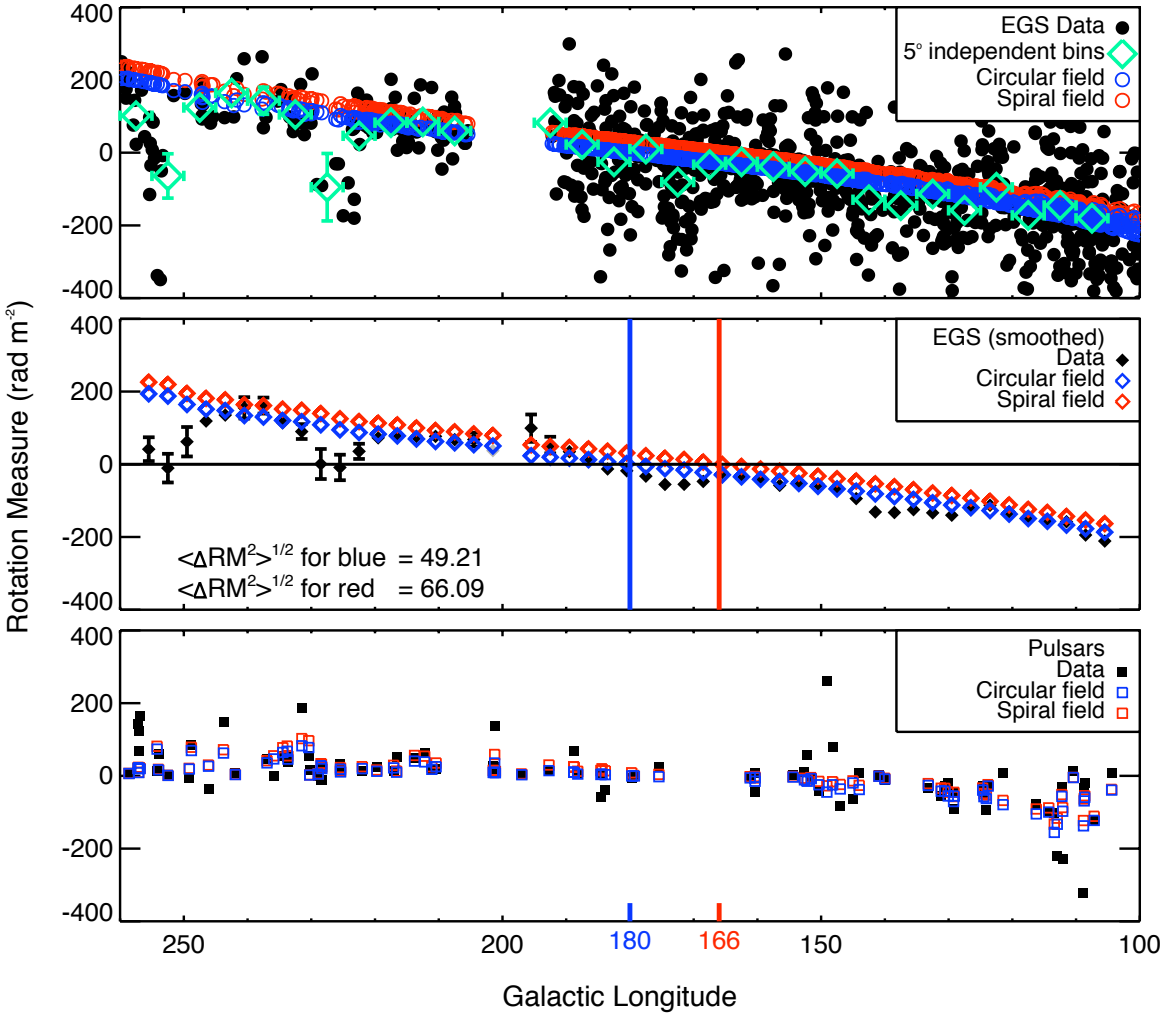

FIG. 7.— Comparison RM versus longitude graphs for observations and models in Sector A. The top panel shows the individual EGS RMs from observations (filled black circles) and those data averaged into 5 degree independent bins (green diamonds). The modeled EGS RMs for the best-fit model based on our circular field are shown as open blue circles, and those for a logarithmic spiral with a pitch angle of 11.5° are shown as open red circles. The middle panel shows the same data as in top panel, except that the corresponding data have been box-car averaged over 9° in longitude with a step size of 3°. Bin symbols in the middle panel shaded grey indicate bins with fewer than 5 sources. The mean [median] number of sources per bin is 47 [56]. The green and blue vertical lines show the corresponding RM null points for the two different modeled RM data sets. The bottom panel shows the RMs of pulsars for observations and the same models.

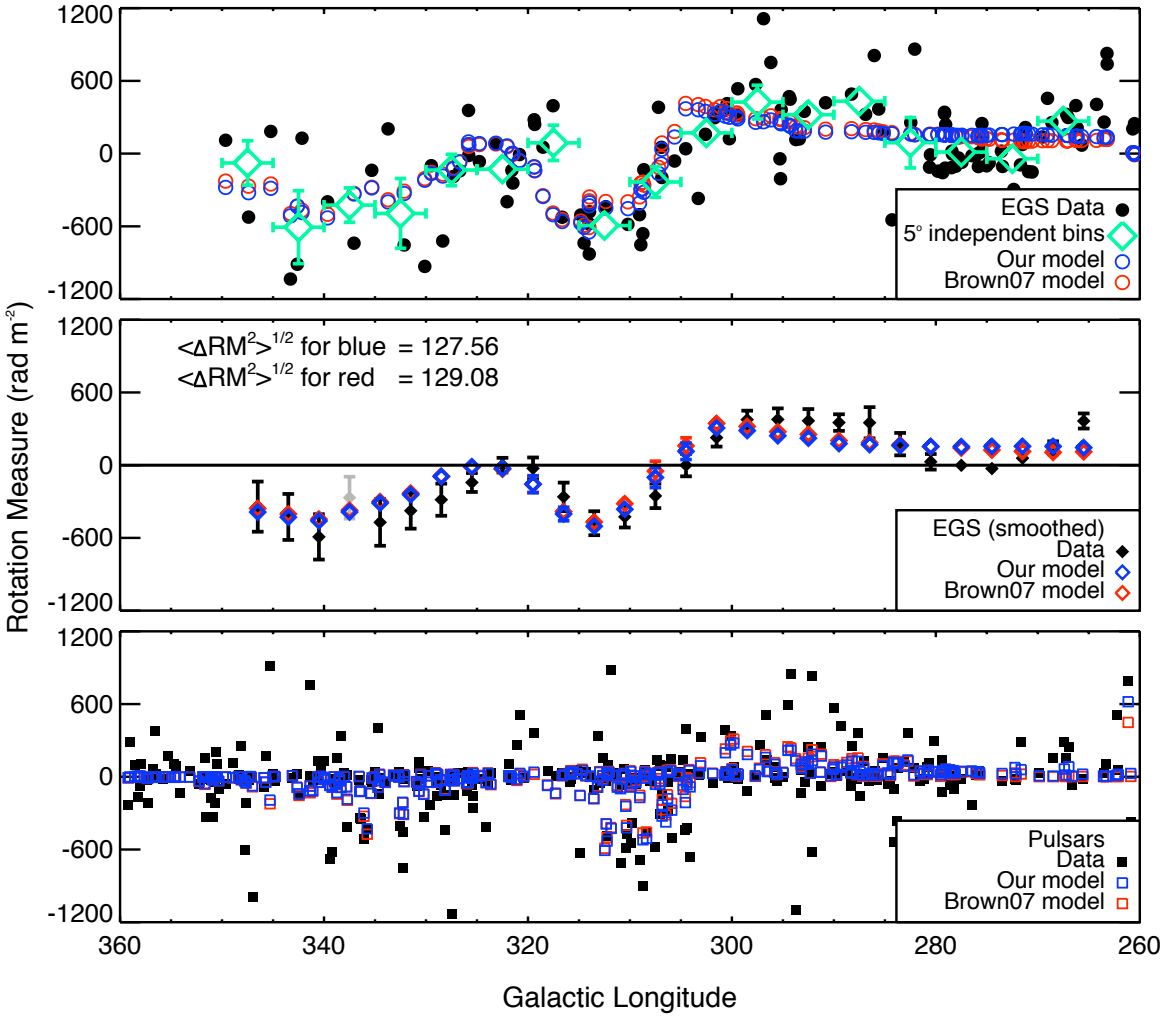

FIG. 8.— Comparison RM versus longitude graphs for observations and models in Sector B. The panels are the same as in Figure 7 with the comparative model (in red) being that from Brown et al. (2007) and our model (in blue) as described in the text. The mean [median] number of sources per bin in the middle panel is 12 [12].

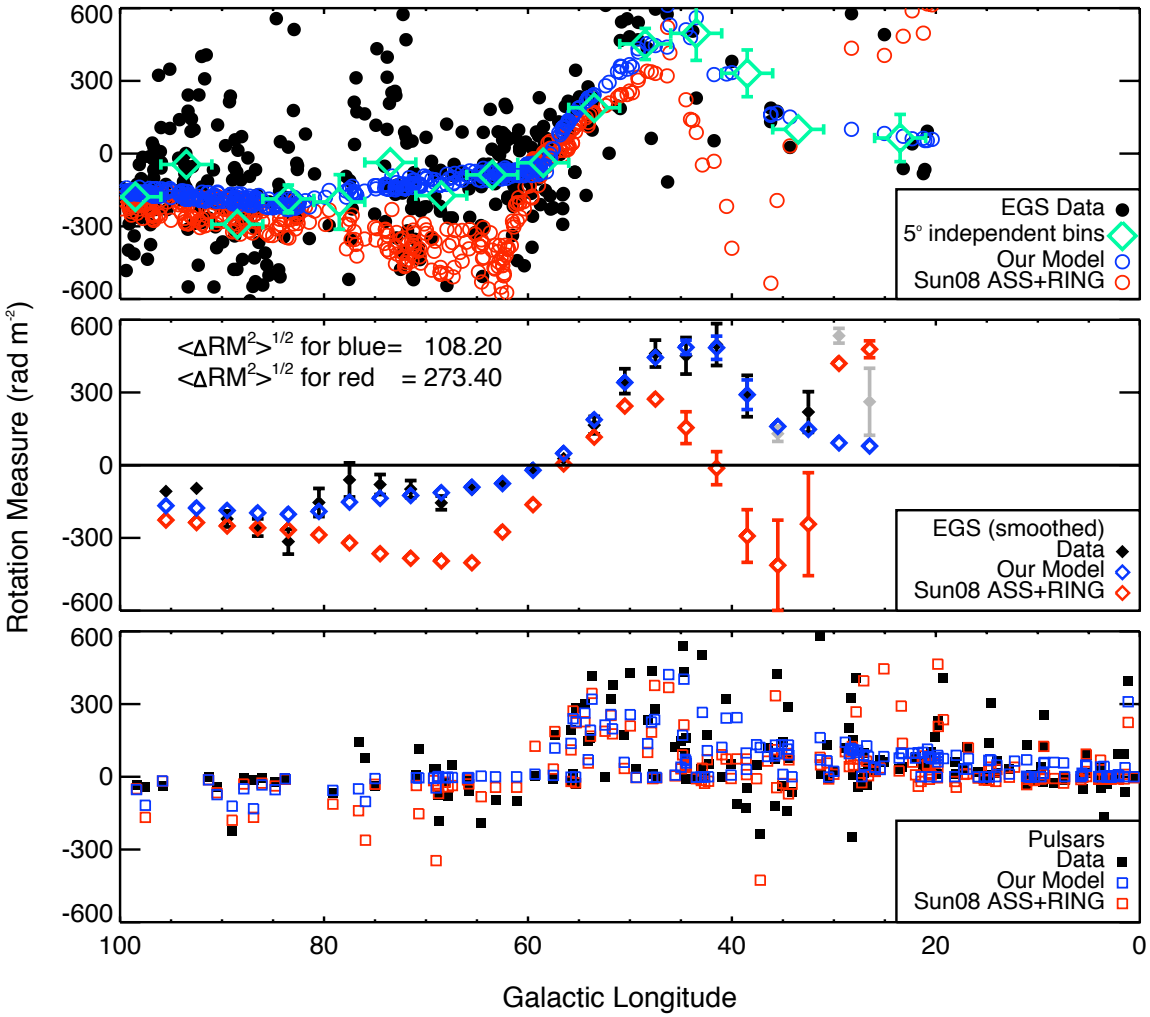

FIG. 9.— Comparison RM versus longitude graphs for observations and models in Sector C. The panels are the same as in Figure 7 with the comparative model (in red) being that from Sun et al. (2008) and our model (in blue) as described in the text. The mean [median] number of sources per bin in the middle panel is 44 [49].

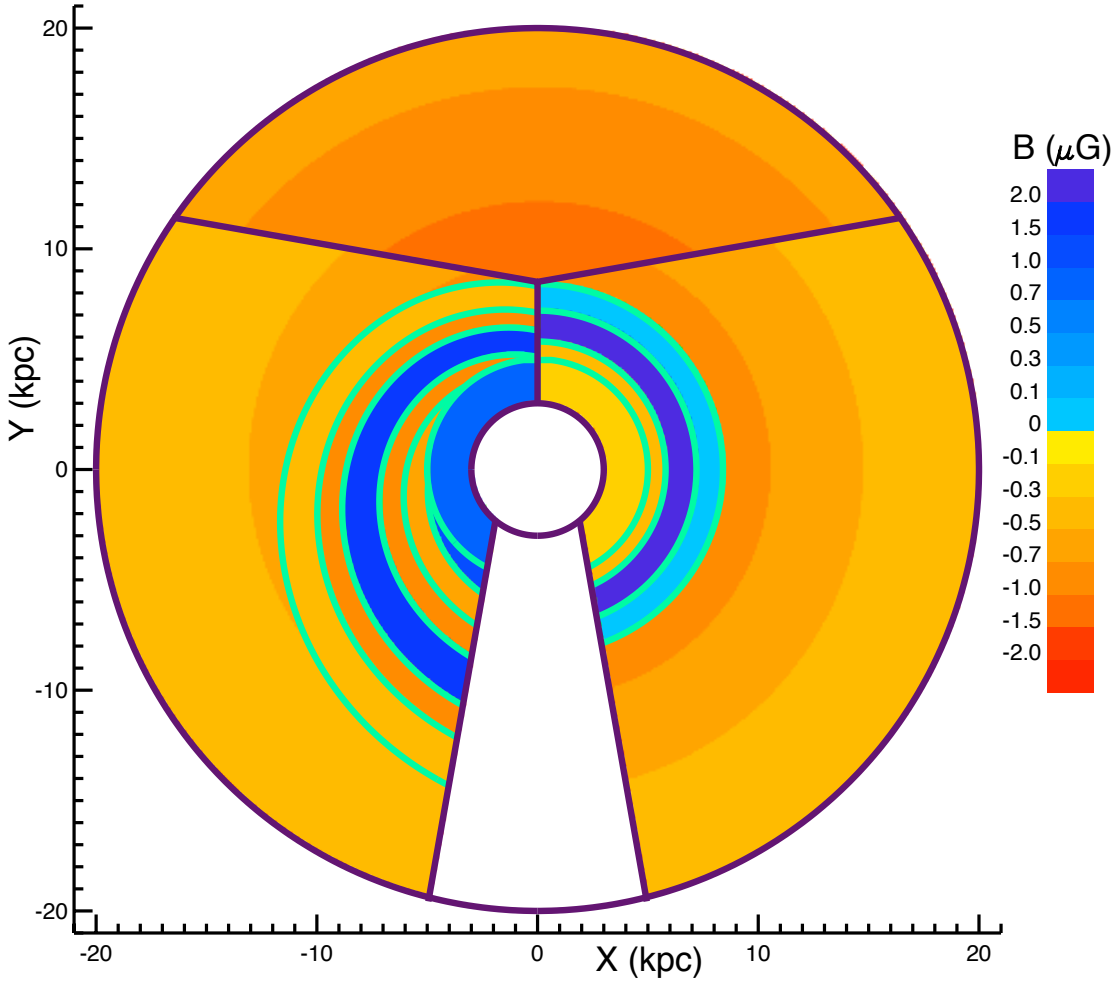

FIG. 10.— Best-fit magnetic field strengths for each of the regions shown in the lower panel of Figure 6. Shades of orange/red represent clockwise field, while shades of blue represent a counter-clockwise field.

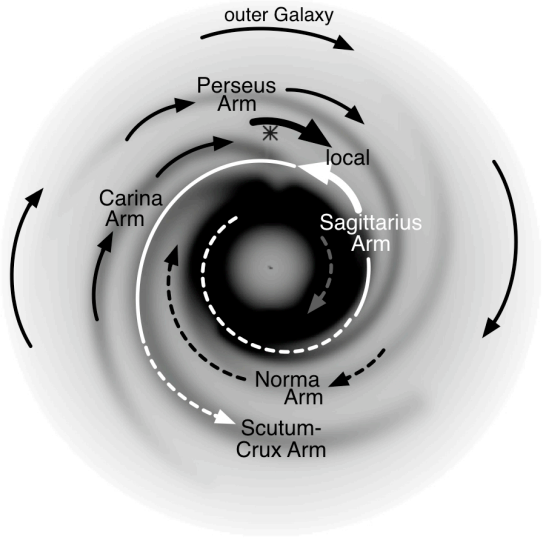

FIG. 11.— A sketch of the magnetic field in the disk of the Galaxy based on this work. The bold arrows in the local arm and Q1 of the Sagittarius-Carina arm shows the only generally accepted location of the large-scale reversal in Q1 (see discussion in Brown 2011). The remaining arrows show the field directions as concluded from this study. The dashed arrows are less certain due to the paucity of data available in these regions.

5. SUMMARY AND DISCUSSION

We have processed a set of VLA observations and produced a catalog of 194 rotation measures of extragalactic sources in the Galactic disk, filling in critical gaps in rotation measure coverage between the Canadian Galactic Plane Survey and the Southern Galactic Plane Survey. Using these data, we conclude that of the three popular models investigated by Sun et al. (2008), the most consistent with our new data is the ASS+RING model.

We propose our own model, stemming from a new modeling strategy that studies the disk field in three different sectors. The division of sectors is roughly between the outer Galaxy (quadrants 2 and 3), quadrant 1 and quadrant 4. Our modeling suggests that the inner Galaxy has a spiral magnetic field that is aligned with the spiral arms, while the outer Galaxy is dominated by an almost purely azimuthal field. This is consistent with a significant decrease of the magnetic pitch angle with the galactocentric radius, to small (almost zero) values beyond the Solar orbit. Such a decrease is also seen in external spiral galaxies (Fig. 8 in Beck et al. 1996). For example, the pitch angle in M31 decreases from $-19 \pm 3^\circ$ near the galactic center to $-8 \pm 3^\circ$ at $r = 12$–14 kpc (Fletcher et al. 2004).

Our model also indicates that the magnetic field in the Galaxy is predominantly clockwise, with a single reversed region that appears to spiral out from the center of the Galaxy. This is similar to the ASS+ARM model described by Sun et al. (2008), except that the pitch angle varies with radius in our model. In some sense, our model provides a 'unification' of the two axisymmetric spiral models discussed by Sun et al. (2008).

The origin of magnetic reversals remains poorly understood. An obvious possibility to explain them is a bisymmetric magnetic field (perhaps of primordial origin; see Sofue et al. 1986, and references therein). A bisymmetric magnetic structure has reversals between spiral-shaped regions, i.e., both in radius and azimuth. However, it is now believed that bisymmetric magnetic fields are rare in spiral galaxies, and that galactic magnetic fields are maintained by some form of dynamo action (Beck et al. 1996). Dynamo mechanisms generally favor axisymmetric magnetic structures, with non-axisymmetric features resulting from secondary effects (such as the spiral pattern and/or overall galactic asymmetry). Our results indicate that the regular magnetic field in the outer part of the Milky Way is predominantly axisymmetric. Ruzmaikin et al. (1985) suggested that radial reversals of an axisymmetric magnetic field can be maintained, for periods comparable to the galactic lifetime, provided the initial (seed) magnetic field had such reversals, for example if the seed field was random (resulting, e.g., from the fluctuation dynamo action). Ruzmaikin et al. (1985) confirmed that a few reversals can persist in the Milky Way if the half-thickness of the ionized layer is within the range 350–1500 pc, whereas this range is much narrower in the case of M31, 350–450 pc (these estimates can be model-dependent). This seems to explain the presence of at least one reversal in the Milky Way and their absence in M31. Asymptotic analysis of the mean-field galactic dynamo equations with α-quenching (Belyanin et al. 1994) shows that the radial reversals can be persistent at those galactocentric radii r where

$$r^2\gamma(r)\left(\frac{1}{r}+2\frac{B_0'(r)}{B_0(r)}\right)+\frac{1}{2}r^2\gamma'(r)=0,$$

where $\gamma(r)$ is the local growth rate of the regular magnetic field due to the dynamo action, $B_0(r)$ is its local saturation strength (presumably corresponding to the energy equipartition with the turbulent energy), and prime denotes derivative with respect to radius (see Shukurov 2005, for a review). Thus, the occurrence of the reversals is sensitive to rather subtle details of the galactic dynamo that are poorly known. This severely restricts the predictive power of the theory and limits the value of numerical results, which are inevitably obtained with idealized and often heavily parameterized models.

As another way to visually examine our modeling efforts, we have combined our 3 magnetic sectors with NE2001 to produce a rotation measure map at $z = 0$, as shown in Figure 12. The small circles along the interior show the pulsar RMs, and the larger circles around the outside (at $R = 20$ kpc) are the smoothed (9° bin widths, 3° steps between bins) EGS RMs, corresponding to the middle plot in Figures 7 through 9. While certainly there are places where the data and the model disagree in Figure 12 (likely due to small scale fluctuations in the data that have not been accounted for and perhaps also due to the limitations of the model), overall the data appears to be fitted quite well. Were it not for the black circles on the data points, many of these points would be virtually indistinguishable from the background model.

We expect that significant improvements on this model, using the same technique and the present edition of the electron density model, will be difficult to accomplish for several reasons. First, the electron density model includes very little small scale structure beyond the local regions. Second, the reliability of distances to the pulsars remains questionable; small shifts in the assumed position of the pulsars will influence the results of the best fit. Fortunately, the EGS are simply assumed to be located at the edge of the Galaxy in their identified ℓ, b direction, making their 'position' reliable. Therefore, they can provide a stable base to assess the model. Finally, as is always the case with modeling, more data would vastly improve the model. For example, pulsars on the far side of the Galactic center would provide much needed constraints

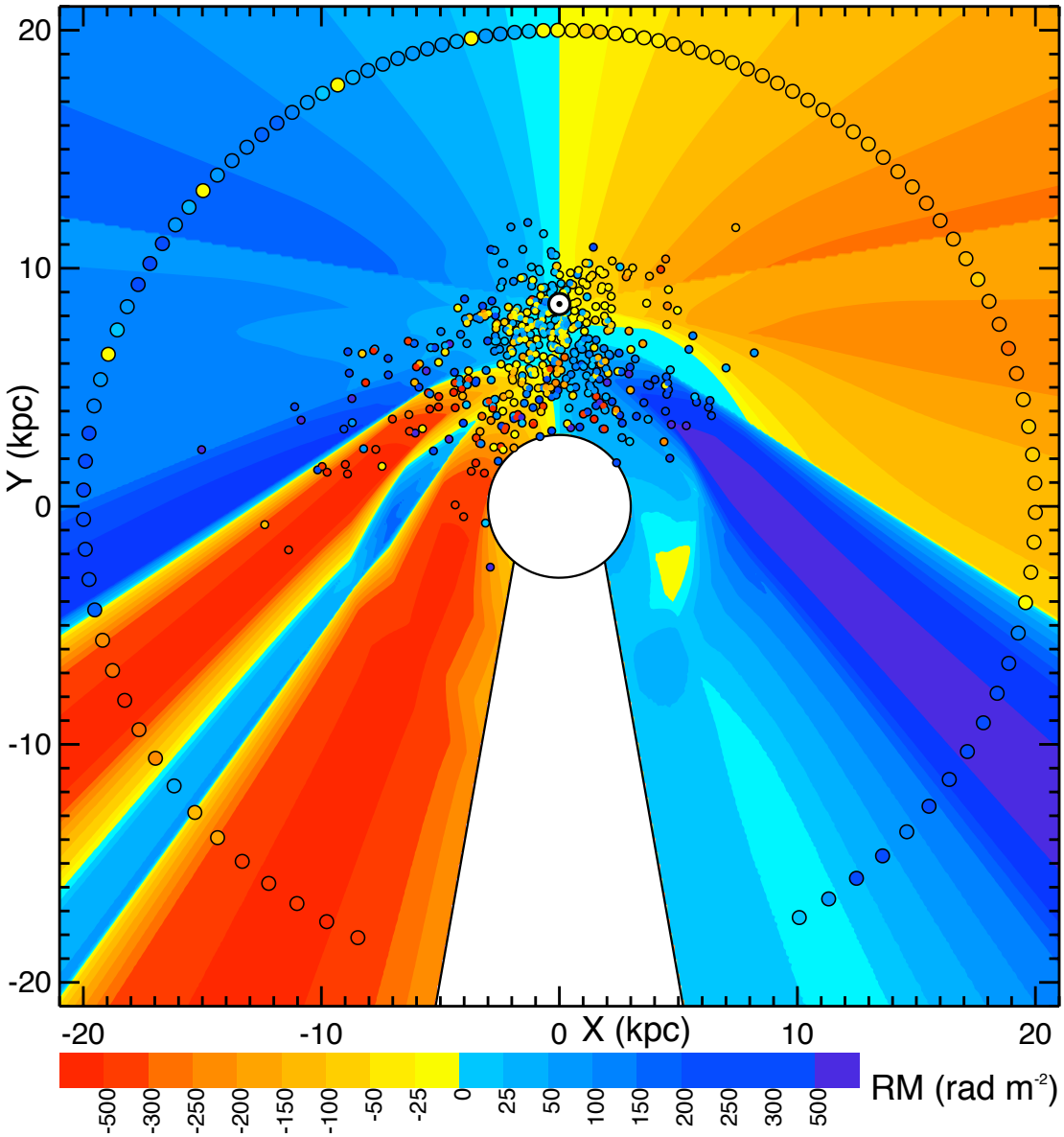

FIG. 12.— Predicted rotation measures for a slice of the Galaxy at z=0 using our 3 sector model as illustrated in the lower panel of Figure 6, and Figure 10. The smaller circles represent RMs for individual pulsars, while the large circles represent RMs for boxcar-averged EGS sources over 9° longitude with a step size of 3°. The EGS are placed at the edge of our model (R = 20 kpc). The central black circle is the inner edge of the molecular ring (R = 3 kpc).

in the area, and as discussed above, the EGS source density is considerably lower in this part of the inner Galaxy as well. However, such data are unlikely to be available until higher sensitivity instruments, such as ASKAP or the SKA come online. While more work and more observations are needed to confirm our findings, we believe that our approach to empirical modeling yields a more reasonable model than attempting to model the entire Galaxy with the current status of both the electron density and available data.

We thank the referee for many insightful comments and suggestions that have significantly improved this manuscript. We also thank Rick Perley and the other staff at the NRAO for their assistance in collecting and processing the data. This work was supported in part by a grant to J.C.B. from the Natural Sciences and Engineering Research Council of Canada. B.M.G. acknowledges the support of an Australian Research Council Federation Fellowship through grant FF0561298. The National Radio Astronomy Observatory is a facility of the National Science Foundation operated under cooperative agreement by Associated Universities, Inc.

REFERENCES

Beck, R., Brandenburg, A., Moss, D., Shukurov, A., & Sokoloff, D. 1996, ARA&A, 34, 155
Beck, R. 2007, A&A, 470, 539
Belyanin, M. P., Sokoloff, D. D., & Shukurov, A. M. 1994, Russ. J. Math. Phys., 2, 149
Brentjens, M. A., & de Bruyn, A. G. 2005, A&A, 441, 1217
Brown, J. C., Taylor, A. R. 2001, ApJ, 563, L31
Brown, J. C. 2002, Ph.D. Thesis, University of Calgary, Canada
Brown, J. C., Taylor, A. R., & Jackel, B. J. 2003, ApJS, 145, 213
Brown, J. C., Taylor, A. R., Wielebinski, R., & Mueller, P. 2003, ApJ, 592, L29
Brown, J. C., Haverkorn, M., Gaensler, B. M., Taylor, A. R., Bizunok, N. S., McClure-Griffiths, N. M., Dickey, J. M., & Green, A. J. 2007, ApJ, 663, 258
Brown, J.C. 2011 in The Dynamic ISM: A Celebration of the Canadian Galactic Plane Survey, edited by R. Kothes, T.L. Landecker, & A.G. Willis, Astron. Soc. Pacific. Conf. Ser., 438, 216
Condon, J. J., Cotton, W. D., Greisen, E. W., Yin, Q. F., Perley, R. A., Taylor, G. B., & Broderick, J. J. 1998, AJ, 115, 1693
Cordes, J. M., & Lazio, T. J. W. 2002, arXiv:astro-ph/0207156v3
Farnsworth, D., Rudnick, L., Brown, S. 2011, ApJ, *submitted*
Fletcher, A., Berkhuijsen, E. M., Beck, R., & Shukurov, A. 2004, A&A, 414, 53
Gaensler, B. M., Madsen, G. J., Chatterjee, S., & Mao, S. A. 2008, Publications of the Astronomical Society of Australia, 25, 184
Goldstein, S. J., Jr., & Reed, J. A. 1984, ApJ, 283, 540
Han, J. L., and Qiao, G. J. 1994, AAP, 288, 759
Han, J. L., Manchester, R. N., & Qiao, G. J. 1999, MNRAS, 306, 371
Han, J. L., Manchester, R. N., Lyne, A. G., Qiao, G. J., & van Straten, W. 2006, ApJ, 642, 868
Haverkorn, M., Gaensler, B. M., McClure-Griffiths, N. M., Dickey, J. M., & Green, A. J. 2006, ApJS, 167, 230
Haverkorn, M., Gaensler, B. M., Brown, J. C., Bizunok, N. S., McClure-Griffiths, N. M., Dickey, J. M., & Green, A. J. 2006, ApJ, L33
Haverkorn, M., Brown, J. C., Gaensler, B. M., & McClure-Griffiths, N. M. 2008, ApJ, 680, 362
Heald, G., Braun, R., & Edmonds, R. 2009, A&A, 503, 409
Jansson, R., Farrar, G. R., Waelkens, A. H., & Enßlin, T. A. 2009, Journal of Cosmology and Astro-Particle Physics, 7, 21
Kothes, R., & Brown, J.-A. 2009, IAU Symposium, 259, 75
Kronberg, P. P., & Newton-McGee, K. J. 2009, arXiv:0909.4753
Mao, S. A., Gaensler, B. M., Haverkorn, M., Zweibel, E. G., Madsen, G. J., McClure-Griffiths, N. M., Shukurov, A., & Kronberg, P. P. 2010, ApJ, 714, 1170
Men, H., Ferrière, K., & Han, J. L. 2008, A&A, 486, 819
Menke, W. 1984, "Geophysical Data Analysis: Discrete Inverse Theory", Academic Press, inc.
Mitra, D., Wielebinski, R., Kramer, M., & Jessner, A. 2003, A&A, 398, 993
Nota, T., & Katgert, P. 2010, A&A, 513, A65
Noutsos, A., Johnston, S., Kramer, M., & Karastergiou, A. 2008, MNRAS, 386, 1881
Poezd, A., Shukurov, A. and Sokoloff, D. 1993, MNRAS, 264, 285
Rae, K.M. & Brown, J.C. 2011 in The Dynamic ISM: A Celebration of the Canadian Galactic Plane Survey, edited by R. Kothes, T.L. Landecker & A.G. Willis, Astron. Soc. Pacific. Conf. Ser., 438, 229
Roy, S., Rao, A. P., & Subrahmanyan, R. 2005, MNRAS, 360, 1305
Ruzmaikin, A., Sokoloff, D., & Shukurov, A. 1985, A&A, 148, 335
Ruzmaikin, A., Sokoloff, D., & Shukurov, A. 1988, Nature, 336, 341
Shukurov, A. 2005, in: Cosmic Magnetic Fields, eds. R. Wielebinski & R. Beck, Lect. Notes Phys. 664, Springer, Berlin–Heidelberg, 2005, pp. 113Ű-135.
Simard-Normandin, M. & Kronberg, P.P. 1980, ApJ, 242, 74
Sofue, Y., Fujimoto, M., & Wielebinski, R. 1986, ARAA, 24, 459
Sokoloff, D. D., Bykov, A. A., Shukurov, A., Berkhuijsen, E. M., Beck, R., & Poezd, A. D. 1998, MNRAS, 299, 189
Sun, X. H., Reich, W., Waelkens, A., & Enßlin, T. A. 2008, A&A, 477, 573
Taylor, J. H., Manchester, R. N., & Lyne, A. G. 1993, ApJS, 88, 529
Taylor, A. R., et al. 2003, AJ, 125, 3145
Taylor, A. R., Stil, J. M., & Sunstrum, C. 2009, ApJ, 702, 1230
Vallée, J. P. 2005, ApJ, 619, 297
Vallée, J. P. 2008, ApJ, 681, 303
Weisberg, J. M., Cordes, J. M., Kuan, B., Devine, K. E., Green, J. T., & Backer, D. C. 2004, ApJS, 150, 317

TABLE 1
ROTATION MEASURES FROM NEW VLA OBSERVATIONS

l [°]	b [°]	α [h m s]	δ [° ′ ″]	Stokes I† [mJy]	PI† [mJy]	RM‡ [rad m^{-2}]	RM synthesis [rad m^{-2}]	Taylor RM* [rad m^{-2}]
20.36	-1.67	18 34 20.9	-11 56 37	116	6	-317± 9	-318± 8	–
20.84	-1.66	18 35 6.2	-11 30 32	45	3	92± 11	91± 11	–
21.08	-1.60	18 35 19.6	-11 15 59	299	9	-66± 12	-65± 13	-23.4± 17.6
21.22	-2.26	18 37 59.8	-11 26 27	151	16	-83± 4	-82± 4	-75.7± 6.0
22.32	+1.73	18 25 42.7	-08 37 23	353	10	40± 13	40± 14	56.3± 11.9
23.20	+2.21	18 25 37.6	-07 37 29	307	9	-62± 13	-61± 13	-81.1± 13.7
25.04	-2.65	18 46 30.0	-08 13 33	144	8	491± 8	492± 8	–
28.27	-2.24	18 50 54.2	-05 09 42	214	8	577± 10	575± 11	–
34.30	+2.44	18 45 13.6	+02 19 54	36	4	25± 7	27± 7	–
35.57	+1.40	18 51 14.5	+02 59 39	501	9	175± 19	175± 21	34.6± 14.1
36.18	+1.44	18 52 13.4	+03 32 55	222	12	188± 7	188± 7	-458.4± 8.7
36.20	-0.35	18 58 37.8	+02 45 18	95	4	132± 11	133± 11	–
40.01	+1.02	19 00 43.4	+06 45 46	151	12	380± 5	380± 6	-252.3± 13.4
40.10	-3.61	19 17 25.5	+04 42 36	192	6	107± 14	105± 13	–
40.52	+1.71	18 59 12.3	+07 32 14	140	4	625± 14	625± 14	–
41.75	-3.27	19 19 17.3	+06 19 42	262	3	53± 32	55± 34	–
42.88	-3.59	19 22 33.9	+07 10 48	122	2	78± 20	75± 22	–
42.89	+0.57	19 07 41.9	+09 07 17	662	22	703± 12	703± 12	–
43.49	-2.30	19 19 6.3	+08 19 20	82	7	229± 6	230± 6	191.5± 15.7
43.58	+3.74	18 57 31.2	+11 10 53	103	14	525± 4	524± 4	–
43.84	-1.44	19 16 41.2	+09 01 47	35	5	505± 6	504± 7	–
44.06	+3.33	18 59 52.5	+11 25 14	112	7	655± 7	655± 8	–
44.51	+2.60	19 03 23.2	+11 29 5	270	45	831± 3	831± 3	141.3± 7.4
46.09	+1.59	19 10 0.4	+12 25 24	197	7	783± 11	783± 11	–
46.14	-3.76	19 29 22.8	+09 59 1	711	50	24± 6	24± 6	686.6± 7.0
46.31	-0.38	19 17 33.9	+11 42 15	122	7	-117± 8	-117± 8	529.2± 11.6
46.35	+3.09	19 05 1.7	+13 20 47	228	9	575± 10	577± 10	–
47.50	+2.17	19 10 31.9	+13 58 10	162	7	596± 9	597± 9	–
47.91	-1.78	19 25 40.8	+12 27 38	214	7	63± 12	63± 13	–
48.12	-3.98	19 34 0.2	+11 35 50	61	2	-426± 17	-426± 18	–
48.31	-1.37	19 24 58.7	+13 00 33	151	8	435± 8	436± 8	–
48.39	+3.62	19 06 55.4	+15 23 42	131	16	629± 4	629± 4	-37.5± 10.1
49.18	+1.36	19 16 44.2	+15 03 49	425	16	541± 10	542± 11	-145.5± 8.8
49.21	-0.97	19 25 17.3	+13 59 19	784	43	470± 7	470± 7	442.5± 3.6
49.72	-3.56	19 35 38.0	+13 11 44	29	2	-34± 12	-34± 13	–
49.75	+3.75	19 09 1.0	+16 39 44	489	19	451± 10	451± 10	-235.4± 7.9
49.77	+2.86	19 12 19.9	+16 16 28	464	23	751± 8	751± 8	41.7± 8.2
50.04	+2.06	19 15 49.7	+16 08 34	128	7	482± 7	482± 8	–
50.28	+2.61	19 14 14.5	+16 36 40	276	13	556± 8	556± 9	-123.7± 15.9
50.82	+1.19	19 20 32.3	+16 25 57	76	7	543± 6	542± 6	–
50.94	+0.84	19 22 3.8	+16 22 43	246	11	466± 9	466± 9	-228.1± 10.7
50.95	-2.18	19 33 6.4	+14 56 24	414	10	186± 15	187± 16	137.0± 11.8
51.22	-1.42	19 30 52.8	+15 32 35	709	12	196± 22	196± 23	–
52.04	-2.67	19 37 4.8	+15 39 19	256	13	1± 8	1± 8	-37.9± 11.1
53.54	+3.13	19 18 39.3	+19 44 4	753	127	228± 3	228± 3	215.7± 0.9
53.70	+3.30	19 18 20.7	+19 57 52	140	13	161± 5	161± 5	160.5± 10.6
53.96	+3.13	19 19 29.9	+20 06 29	258	10	114± 10	114± 10	129.9± 13.0
54.95	+2.30	19 24 36.9	+20 35 21	583	37	234± 6	234± 6	207.5± 2.3
55.34	+3.95	19 19 8.6	+21 42 58	63	12	212± 3	212± 3	203.1± 8.1
55.40	-2.58	19 43 41.5	+18 37 20	137	7	-76± 8	-77± 8	-120.5± 17.0
55.56	+2.26	19 25 59.5	+21 06 26	1650	42	206± 15	206± 15	217.4± 2.9
55.64	+0.32	19 33 25.4	+20 14 59	78	5	152± 8	152± 9	–
56.08	+0.10	19 35 10.4	+20 31 54	293	9	67± 12	67± 13	–
56.18	-0.57	19 37 54.5	+20 17 30	114	3	96± 15	97± 16	–
56.59	-2.39	19 45 29.9	+19 44 37	161	9	-227± 8	-228± 8	-200.7± 14.3
56.60	-1.11	19 40 46.6	+20 23 51	97	2	-170± 26	-171± 27	–
56.62	+0.17	19 36 2.4	+21 01 47	143	3	117± 18	115± 19	–
56.85	+0.97	19 33 31.4	+21 37 38	134	9	-4± 6	-4± 7	–
57.58	+1.93	19 31 24.9	+22 43 32	568	19	53± 11	53± 12	28.4± 5.4
57.83	-2.36	19 48 0.7	+20 50 26	427	35	-174± 5	-174± 5	-206.9± 2.7
58.29	-2.59	19 49 51.7	+21 06 56	172	6	-152± 12	-152± 13	–
58.38	+2.26	19 31 49.2	+23 35 2	42	3	41± 10	42± 10	–
58.48	+2.62	19 30 37.9	+23 50 45	290	9	112± 12	112± 12	74.2± 8.6
58.77	-0.73	19 43 57.6	+22 27 42	133	4	-17± 12	-15± 13	–
58.78	-2.40	19 50 14.6	+21 38 0	127	16	-210± 4	-210± 4	-190.1± 5.9
58.97	+0.20	19 40 50.3	+23 06 5	265	12	73± 8	73± 9	36.9± 6.1
59.03	+1.85	19 34 44.4	+23 57 50	84	3	-105± 14	-110± 15	–
59.17	+2.82	19 31 18.6	+24 33 2	45	2	89± 12	90± 13	–
59.37	+3.21	19 30 15.4	+24 54 29	131	9	2± 7	1± 7	-24.0± 10.3
59.47	+3.57	19 29 2.2	+25 10 35	40	2	-44± 14	-46± 15	–
59.48	+3.42	19 29 39.8	+25 06 26	174	9	-83± 8	-83± 8	-91.6± 12.2
59.48	+1.95	19 35 20.3	+24 24 15	17	3	-79± 9	-80± 9	–
59.60	-0.07	19 43 18.3	+23 30 32	171	9	-387± 8	-387± 8	272.2± 8.6
59.87	-1.35	19 48 41.0	+23 06 8	200	5	-85± 15	-84± 16	–

TABLE 1
– Continued

l [°]	b [°]	α [h m s]	δ [° ′ ″]	Stokes I† [mJy]	PI† [mJy]	RM‡ [rad m^{-2}]	RM synthesis [rad m^{-2}]	Taylor RM* [rad m^{-2}]
60.09	+3.45	19 30 49.3	+25 39 12	170	9	-67± 7	-67± 8	-73.5± 11.5
60.29	+1.89	19 37 19.0	+25 04 31	70	8	-102± 5	-103± 5	-103.5± 12.3
60.44	+1.06	19 40 48.5	+24 47 48	113	5	-54± 10	-53± 10	-19.3± 13.2
60.78	-0.64	19 48 2.0	+24 14 42	337	13	-184± 10	-184± 11	-189.1± 6.9
60.81	+1.59	19 39 34.2	+25 23 20	156	8	24± 8	24± 9	9.2± 11.9
61.07	-2.08	19 54 5.8	+23 45 41	110	9	-154± 6	-155± 6	-165.6± 11.0
61.16	+3.92	19 31 14.7	+26 49 6	172	10	214± 7	214± 8	215.2± 8.8
61.95	+2.39	19 38 58.3	+26 46 12	892	16	58± 21	58± 21	42.4± 4.1
61.98	-2.33	19 57 5.5	+24 24 36	377	9	-179± 15	-180± 16	-20.2± 7.7
62.36	-0.96	19 52 48.7	+25 26 58	1093	40	-96± 11	-96± 11	-106.3± 2.9
62.36	-1.77	19 55 52.2	+25 01 47	494	36	-53± 5	-53± 6	-65.5± 2.9
62.48	+1.42	19 43 56.4	+26 44 56	88	5	86± 8	86± 8	–
205.43	-3.75	06 24 18.8	+04 57 1	371	13	60± 10	61± 11	57.0± 6.3
205.81	+4.91	06 56 1.0	+08 34 7	503	26	26± 8	26± 8	20.1± 4.2
205.92	+3.39	06 50 45.9	+07 47 9	357	9	26± 15	26± 16	-6.8± 5.7
207.14	-1.33	06 36 5.7	+04 32 40	1001	54	59± 7	59± 7	50.2± 1.5
207.37	+3.62	06 54 12.7	+06 35 39	111	7	109± 7	110± 8	–
207.52	+3.25	06 53 9.1	+06 18 10	589	35	128± 7	128± 7	107.2± 2.9
207.82	-4.39	06 26 28.0	+02 31 51	480	21	-17± 9	-17± 9	-0.4± 4.5
207.97	+2.14	06 50 0.7	+05 23 59	92	8	153± 5	153± 6	156.2± 12.0
209.15	-2.62	06 35 10.2	+02 10 9	144	8	112± 7	111± 8	124.5± 7.7
209.25	-4.63	06 28 12.6	+01 09 26	962	30	34± 12	35± 12	38.9± 3.3
209.31	+4.81	07 02 1.7	+05 24 24	157	4	92± 14	94± 15	28.2± 12.4
209.50	+1.10	06 49 4.6	+03 33 51	113	10	-45± 5	-45± 5	-58.1± 8.1
209.59	+2.38	06 53 49.9	+04 03 47	358	14	42± 10	42± 10	39.6± 7.0
210.12	-2.62	06 36 56.6	+01 18 22	419	32	99± 5	99± 5	158.3± 8.1
210.16	-4.08	06 31 51.5	+00 36 14	299	7	7± 15	6± 16	17.2± 10.1
210.51	+1.11	06 50 59.7	+02 39 56	93	9	58± 5	58± 6	58.5± 15.3
211.12	-1.56	06 42 32.0	+00 54 18	99	9	179± 5	180± 6	158.5± 10.7
211.18	+0.85	06 51 16.2	+01 56 51	209	10	81± 9	81± 9	62.2± 11.8
211.26	+2.41	06 56 57.7	+02 35 34	173	10	73± 7	74± 8	60.1± 7.5
211.67	+0.63	06 51 21.9	+01 24 27	298	9	79± 13	79± 13	4.5± 7.9
212.85	-1.78	06 44 56.0	-00 44 17	246	7	187± 13	187± 14	159.5± 14.0
213.14	+4.73	07 08 38.6	+01 58 25	126	4	13± 13	10± 13	–
213.49	+3.62	07 05 17.6	+01 09 30	150	9	57± 7	57± 7	72.1± 12.1
213.84	-3.60	06 40 15.6	-02 26 51	158	8	150± 9	151± 9	173.8± 10.3
214.49	-1.08	06 50 25.7	-01 52 22	457	12	86± 14	86± 15	108.3± 6.4
214.76	+4.53	07 10 53.6	+00 26 48	557	36	29± 6	29± 6	32.1± 2.0
215.05	+2.26	07 03 19.1	-00 51 2	936	23	14± 15	14± 16	17.6± 0.7
215.07	+3.44	07 07 33.8	-00 19 37	207	23	42± 4	42± 4	35.5± 2.3
215.17	+3.99	07 09 42.1	-00 09 56	189	13	38± 6	39± 6	25.6± 5.1
215.65	+3.59	07 09 11.3	-00 46 29	240	17	32± 6	32± 6	31.9± 3.7
215.73	-0.70	06 54 2.6	-02 48 3	318	11	62± 11	62± 12	79.6± 6.9
216.04	+0.40	06 58 32.2	-02 34 37	268	6	103± 16	102± 17	70.4± 10.2
216.50	+1.60	07 03 38.5	-02 26 9	94	9	7± 5	6± 5	4.8± 9.6
216.82	-4.00	06 44 13.9	-05 16 36	210	28	153± 3	152± 3	150.4± 3.0
216.89	+0.18	06 59 18.3	-03 25 51	164	10	88± 7	87± 7	–
217.27	+4.23	07 14 24.2	-01 55 29	191	11	64± 7	65± 8	59.0± 8.0
217.45	+4.78	07 16 42.1	-01 49 21	65	8	122± 5	122± 5	103.0± 11.5
217.48	-1.37	06 54 50.4	-04 40 2	68	6	202± 7	202± 7	–
217.78	-2.95	06 49 45.6	-05 39 22	465	20	88± 9	88± 9	74.0± 5.3
217.96	+4.26	07 15 47.0	-02 31 1	1410	47	110± 11	110± 12	124.9± 2.3
218.01	-3.95	06 46 34.7	-06 18 34	196	12	78± 7	78± 7	69.5± 5.6
218.14	+3.78	07 14 23.8	-02 54 9	172	9	88± 8	89± 8	98.7± 10.9
218.41	+2.50	07 10 20.1	-03 43 26	1158	27	116± 16	115± 17	135.7± 1.6
218.81	+0.52	07 04 2.7	-04 59 22	147	6	88± 10	88± 10	90.8± 9.8
219.19	-4.89	06 45 20.1	-07 47 5	107	10	86± 5	87± 5	70.6± 8.2
219.27	+0.86	07 06 6.4	-05 14 25	262	16	103± 7	103± 7	95.2± 5.3
219.48	+2.79	07 13 20.3	-04 32 27	304	15	74± 8	74± 8	67.8± 5.0
219.60	+3.04	07 14 28.5	-04 31 30	235	9	87± 10	87± 10	95.6± 7.8
219.75	-3.63	06 50 53.0	-07 42 56	396	4	56± 33	56± 36	29.4± 6.7
220.02	+1.34	07 09 11.9	-05 40 59	165	30	69± 3	69± 3	56.3± 3.6
220.07	-4.70	06 47 38.0	-08 29 1	187	9	69± 8	69± 9	44.2± 7.7
220.11	-4.34	06 48 59.5	-08 21 33	272	13	78± 8	78± 9	78.7± 4.9
220.35	-3.93	06 50 55.0	-08 22 55	137	6	55± 10	56± 10	–
220.35	-3.93	06 50 55.0	-08 22 55	132	5	68± 10	69± 11	–
220.42	-4.95	06 47 20.0	-08 54 34	140	8	90± 7	92± 8	91.4± 10.8
220.44	-0.31	07 04 5.3	-06 49 2	158	9	118± 8	119± 8	116.7± 10.1
220.65	+1.53	07 11 2.2	-06 09 22	333	16	94± 8	94± 8	99.8± 10.0
220.79	+0.93	07 09 10.2	-06 33 30	175	6	86± 11	86± 12	–

TABLE 1
– Continued

l [°]	b [°]	α [h m s]	δ [° ′ ″]	Stokes I† [mJy]	PI† [mJy]	RM‡ [rad m^{-2}]	RM synthesis [rad m^{-2}]	Taylor RM* [rad m^{-2}]
221.00	-4.66	06 49 27.8	-09 17 54	200	20	68± 4	68± 5	62.9± 7.2
221.01	-2.36	06 57 46.2	-08 15 19	367	28	78± 5	78± 5	75.7± 2.8
221.06	-2.95	06 55 43.2	-08 34 44	108	6	99± 8	98± 8	–
221.32	+0.84	07 09 50.1	-07 04 21	204	7	145± 12	145± 12	115.2± 11.4
221.54	-2.04	06 59 53.0	-08 35 21	142	5	75± 11	72± 11	81.9± 15.1
222.39	+4.76	07 25 47.6	-06 11 46	220	8	22± 12	23± 12	24.1± 9.8
222.72	-1.74	07 03 8.6	-09 29 56	162	7	164± 10	162± 10	143.6± 10.5
223.07	-4.99	06 52 1.3	-11 17 6	142	5	73± 12	72± 12	55.9± 12.2
223.25	+1.35	07 15 14.9	-08 32 55	89	7	-128± 6	-129± 7	–
223.27	+1.10	07 14 24.4	-08 40 53	113	7	-180± 8	-180± 8	-140.4± 15.7
223.33	-2.21	07 02 35.7	-10 15 5	239	11	67± 9	67± 9	54.9± 9.2
223.54	-2.82	07 00 46.7	-10 43 23	402	22	64± 7	64± 7	51.0± 3.5
223.67	-3.25	06 59 28.8	-11 01 50	110	5	95± 10	96± 10	48.8± 17.1
224.21	+2.65	07 21 44.1	-08 47 13	268	8	-83± 13	-83± 13	-83.8± 8.6
224.98	+2.73	07 23 28.5	-09 25 55	317	11	-173± 11	-173± 11	-106.9± 8.7
225.41	+1.07	07 18 21.0	-10 35 1	173	27	-547± 3	-276± 3	127.5± 4.6
225.75	+4.94	07 32 50.6	-09 03 18	82	10	-31± 4	-31± 4	-37.5± 7.1
226.15	+4.69	07 32 42.4	-09 31 51	215	10	-31± 8	-32± 9	-26.8± 7.0
228.38	+1.26	07 24 44.0	-13 06 46	204	12	-90± 7	-91± 7	-83.4± 9.0
229.12	+1.18	07 25 52.7	-13 48 33	189	7	-88± 11	-87± 12	-90.3± 14.2
229.87	-0.64	07 20 43.6	-15 19 40	684	43	217± 6	217± 6	190.3± 2.3
230.04	+3.34	07 35 29.9	-13 34 50	145	7	81± 9	80± 9	50.2± 7.8
230.09	-0.62	07 21 13.5	-15 30 39	548	30	113± 7	113± 7	66.9± 2.4
230.17	+1.07	07 27 32.5	-14 46 53	281	12	105± 9	104± 9	78.2± 6.7
231.08	+4.21	07 40 42.2	-14 03 46	355	10	50± 13	51± 14	26.1± 5.1
231.20	+1.16	07 29 55.5	-15 38 27	214	14	81± 7	81± 7	80.6± 6.9
231.66	-0.01	07 26 33.3	-16 36 26	121	8	188± 7	188± 7	169.4± 10.8
231.99	+2.75	07 37 16.2	-15 34 6	90	9	87± 5	86± 5	45.9± 5.4
232.66	+1.87	07 35 25.9	-16 34 48	253	12	77± 8	77± 8	42.3± 6.1
232.83	+3.13	07 40 21.2	-16 06 32	266	16	58± 7	58± 7	58.5± 5.0
233.39	-2.60	07 20 22.1	-19 21 12	175	7	98± 10	98± 10	88.0± 11.0
233.53	-1.31	07 25 28.9	-18 52 6	264	17	148± 6	148± 6	136.7± 3.9
234.75	+0.87	07 36 2.4	-18 53 9	319	18	174± 7	174± 7	156.6± 3.3
235.28	-0.43	07 32 16.4	-19 58 58	144	16	142± 4	142± 4	112.1± 4.9
237.10	+1.30	07 42 32.1	-20 43 41	153	10	97± 7	98± 7	90.0± 8.3
237.51	+0.17	07 39 12.5	-21 38 44	147	9	69± 7	69± 7	64.7± 8.8
237.72	+4.34	07 55 2.3	-19 43 27	258	29	264± 4	264± 4	233.6± 2.7
240.53	-3.57	07 31 16.9	-26 06 0	139	8	258± 8	259± 8	235.3± 12.8
241.70	-1.87	07 40 25.7	-26 17 15	257	12	203± 9	205± 9	171.8± 6.0
242.17	+4.39	08 05 12.4	-23 28 55	99	6	98± 8	99± 9	85.4± 12.4
243.61	+3.38	08 04 49.2	-25 13 55	153	11	96± 6	96± 6	58.1± 10.2
245.43	+1.83	08 03 16.0	-27 36 18	138	12	99± 5	98± 5	77.6± 5.2
245.80	+2.01	08 04 51.5	-27 49 11	720	26	81± 10	81± 11	79.0± 2.5
246.98	+2.78	08 10 41.0	-28 23 40	155	6	133± 11	133± 12	64.1± 14.0
247.06	-4.73	07 41 4.7	-32 21 45	161	10	189± 7	188± 7	168.9± 13.6
247.12	+1.27	08 05 15.8	-29 19 50	117	7	93± 7	92± 8	62.9± 9.7
247.13	+3.14	08 12 25.9	-28 19 40	326	18	102± 7	101± 7	99.2± 4.3
247.25	-1.94	07 52 52.3	-31 07 13	421	16	134± 10	135± 11	94.8± 4.9
249.81	-1.92	07 59 14.3	-33 18 0	233	12	163± 8	163± 8	156.3± 8.4
251.59	-2.17	08 02 44.0	-34 56 20	118	6	157± 8	157± 9	136.8± 12.4

NOTE. — † Both Stokes I and PI (Linear polarized intensity) are determined as the average over all 14 channels for the same pixel, being that with the highest PI.
‡ RM calculations are done using the angle fitting algorithm described in the text.
∗ Missing values do not have a corresponding source within 1′.

TABLE 2
BEST FIT B-FIELD VALUES FOR OUR MODEL SECTORS SHOWN IN FIGURE 6.

Sector and Region	Magnetic pitch angle	Radial dependence	B† (in μG)
Sector A			
1	0°	R^{-1}	-1.20±0.48
Sector B			
1	0°	constant	0.85±0.06
2	11.5°	constant	1.0±0.4
3	11.5°	constant	-0.54 ± 0.07
4	11.5°	constant	-0.92 ± 0.06
5	11.5°	constant	1.71 ± 0.06
6	11.5°	constant	-0.90 ± 0.08
7	11.5°	constant	-0.34 ± 0.06
8	0°	R^{-1}	-0.78 ± 0.12
Sector C			
1	0°	constant	-0.15 ± 0.04
2	11.5°	constant	-0.40 ± 0.01
3	11.5°	constant	2.23 ± 0.13
4	11.5°	constant	0.09 ± 0.05
5	0°	R^{-1}	-0.86 ± 0.09

NOTE. — † Indicated field strengths for R^{-1} regions are values at a Galactocentric radius of 8.5 kpc (ie. at the Sun.) Positive values correspond to a counter-clockwise field as viewed from the north Galactic pole, while negative values correspond to a clockwise field.